ELSEVIER

Volume 184, Issue 5, May 2011

JOURNAL OF SOLID STATE CHEMISTRY

www.elsevier.com/locate/jssc

CONTENTS

Abstracted/indexed in BioEngineering Abstracts, Chemical Abstracts, Coal Abstracts, Current Contents/Physics, Chemical, & Earth Sciences, Engineering Index, Research Alert, SCISEARCH, Science Abstracts, and Science Citation Index. Also covered in the abstract and citation database SCOPUS®. Full text available on ScienceDirect®.

Regular Articles

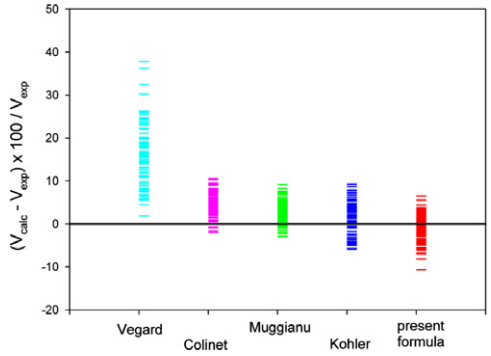

Synopsys: the volume of a ternary intermetallic compound can be calculated starting from volumes of some binary phases, selected by the methods of Colinet, Muggianu, Kohler and a new method proposed here. The so obtained values are compared with the experimental ones for eight ternary systems.

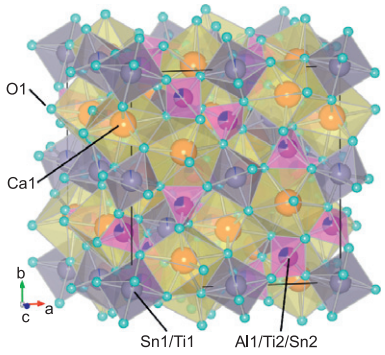

Garnet-type solid solutions of $Ca_3Sn_{3-x}Ti_xAl_2O_{12}$ ($x = 0.6$–1.4) were prepared. Sn^{4+} and Ti^{4+} partially occupy both tetrahedral and octahedral sites. The solid solutions showed a broad emission band peaking at 465 nm under UV excitation.

Regular Articles—Continued

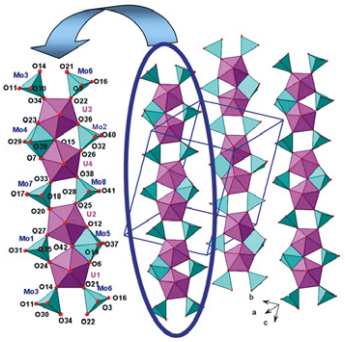

The staking of $^1_\infty[(UO_2)_2(MoO_4)_3(MoO_5)]^{6-}$ infinite uranyl molybdate ribbons in the $Cs_6[(UO_2)_2(MoO_4)_3(MoO_5)]$ structure.

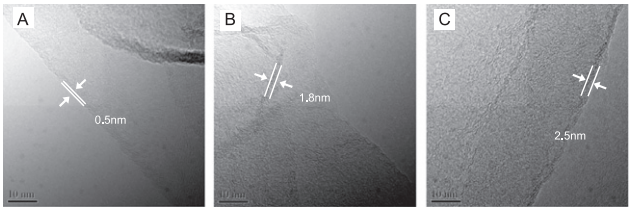

The typical TEM images of the graphene sheets derived from GO3(a), GO2(b) and GO1(c).

Continued

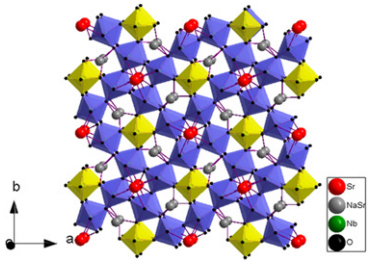

Representation of the unit cell of the NaSr2Nb5O15 powder. Nb^{5+} cations are differentiated as Nb(I) and Nb(II). [Nb(I)O6] octahedral sites are represented by yellow color and [Nb(II)O6] by blue ones.

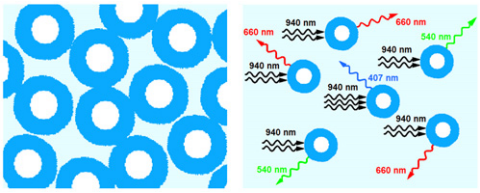

A highly viscous shell (shown in the picture in dark blue) is build around the growing crystal (white circles). When the shell's T_g approaches the annealing temperature, the crystal growth is fully suppressed for kinetic reasons. The upconversion luminescence, resulting from the simultaneous absorption of two and even three infrared photons, is depicted schematically in the right part of the figure.

Schematic illustration of the growth of calcite aggregates with different morphologies obtained from (a) Low G alginate gels and (b) High G alginate gels.

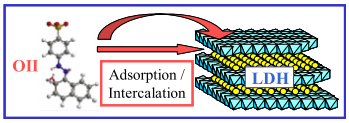

Structural and thermodynamical insight of adsorption/Intercalation of OII in Mg_RAl LDH.

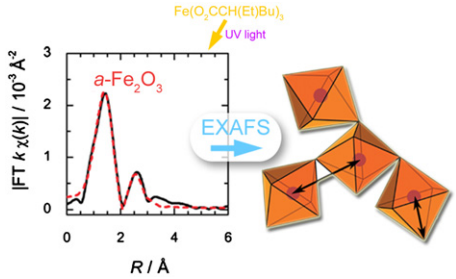

Using X-ray absorption fine structure spectroscopy, the oxidation state and local order of metal oxides produced from the solid-state photochemical decomposition of metal 2-ethylhexanoates (metal = Co, Fe, Cr) is presented.

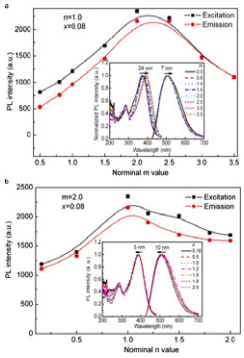

Dependence of photoluminescence intensity and normalized photoluminescence spectra (the inset) of Ca-α-Sialon:Ce^{3+},Li^+ on the host lattice composition: (a) *m* value and (b) *n* value.

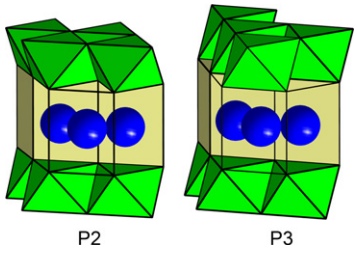

Polyhedral presentation of layered structures of $Na_x[Cr_{(1+x)/2}Sb_{(1-x)/2}]O_2 \cdot$ ($Cr,Sb)O_6$ octahedra are green. Part of the sodium prisms are open to show short distances between sodium sites which cannot be occupied simultaneously.

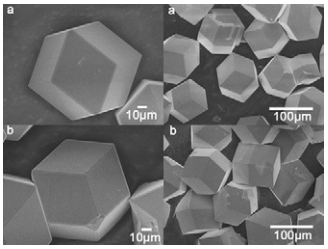

The two single crystals $Pr_3Fe_5O_{12}$ (a) and $Nd_3Fe_5O_{12}$ (b) were successfully synthesized via mild hydrothermal route.

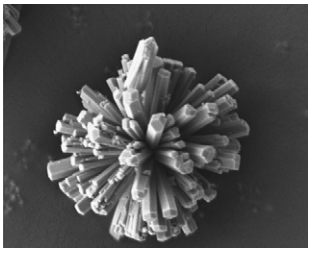

Zinc germanate materials were synthesized possessing unique morphologies dependent on the hydrothermal synthesis conditions in the absence of surfactant, catalyst or template. These novel materials are characterized and evaluated for their photocatalytic activities.

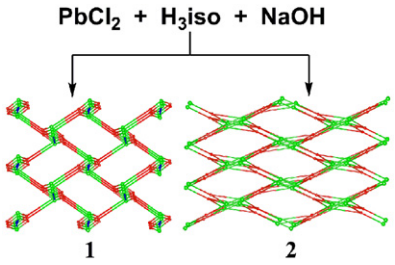

The reactions of $PbCl_2$ with 2,4-dioxo-1,2,3,4-tetrahydropyrimidine-5-carboxylic acid (H_3iso) gave two complexes $[Pb(H_2iso)_2(H_2O)]_n$ (**1**) and $[Pb(Hiso)(H_2O)]_n$ (**2**), which display different topologies and fluorescent properties.

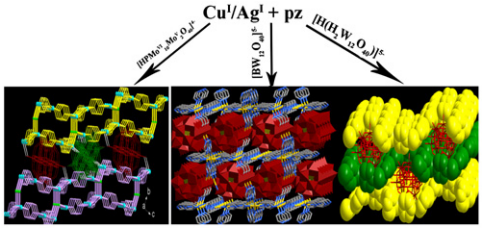

The choice of the particular Keggin template is shown to influence the structural properties of the Cu/Ag PCPs. Their photocatalytic activities have been studied.

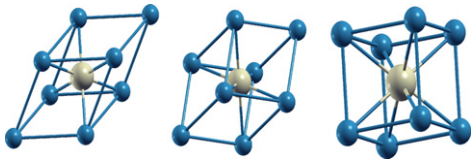

Pressure induced transition from the B1 structure (left) via the transition state (middle) to the B2 structure (right).

Continued

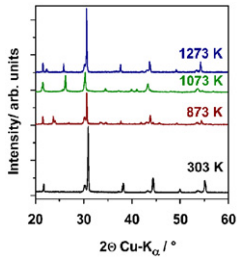

In-situ XRD of BCFZ powder in the atmosphere containing 50% CO_2 and 50% N_2 at different temperatures showing formation of $BaCO_3$ and their phase transition.

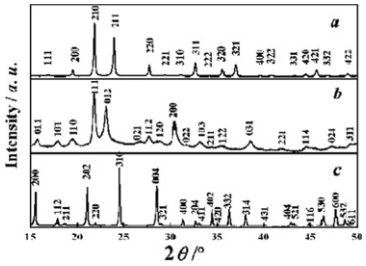

A novel cubic $ZrW_{1.80}V_{0.20}O_{7.90}$ solid solution (*a*) was synthesized through its metastable orthorhombic phase (*b*) as the dehydration product of hydrate precursor $ZrW_{1.80}V_{0.20}O_{6.90}(OH)_{2.00}(H_2O)_{2.00}$ (*c*).

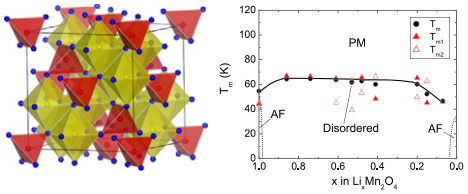

Magnetic phase diagram of the chemically delithiated spinel $Li_xMn_2O_4$ determined by magnetic susceptibility (χ) and muon spin rotation/relaxation (μSR) measurements.

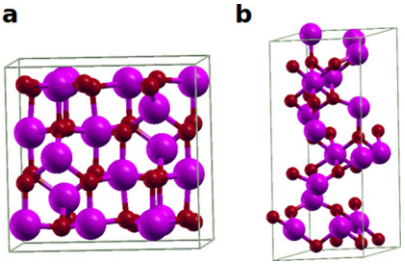

Two γ-Alumina bulk models selected in this work for a comparison focusing in the electronic structure and thermodynamics of the systems. (a) The nonspinel model and (b) the spinel-like model.

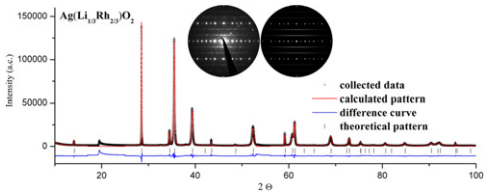

Two new quaternary delafossite type oxides with the general formula $Ag(Li_{1/3}M_{2/3})O_2$, M = Rh, Ir, have been synthesized, and their structures characterized. The real structures of the quaternary delafossites have been revealed, which has allowed to fully explain the diffuse scattering as observed in X-ray powder diffraction.

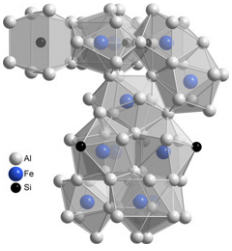

Partial representation of the crystal structure of the α-$Al_{7.1}Fe_2Si$ compound.

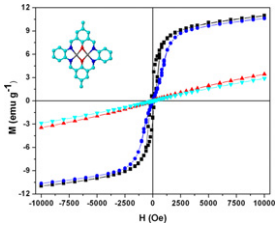

Microwave assisted synthesis was used to obtain an intercalated $MnPS_3$ phase with a binuclear Zn(II) macrocyclic complex. A comparative magnetic study of the composites obtained by assisted microwave and traditional synthetic methods is reported.

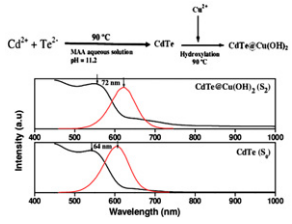

Schematic of aqueous synthesis route for $CdTe@Cu(OH)_2$ nanocomposite and The Stokes shift of CdTe nanocrystals and $CdTe@Cu(OH)_2$ Nanocomposites, (CdTe: emission at 605 nm, $CdTe@Cu(OH)_2$: emission at 621 nm).

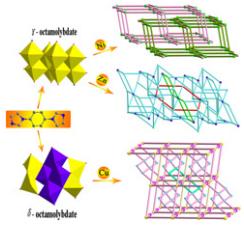

With BIMB ligand, we have obtained and characterized three novel POM-based entangled hybrid compounds. Compound **1** is a 2-fold interpenetration 3D framework; **2** and **3** exhibit self-penetrating 3D polycatenated frameworks.

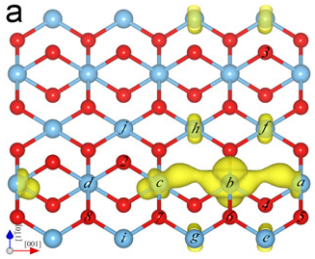

The study investigates the magnetic properties of the oxygen-deficient rutile TiO_2(1 1 0) surface from first principle calculations. The adjacent oxygen vacancies form a ferromagnetic arrangement due to the double exchange interaction.

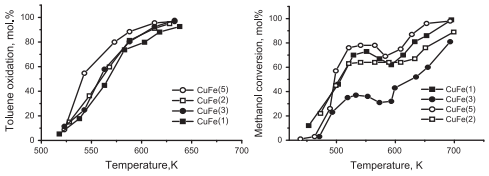

It is demonstrated that the catalytic behavior of the obtained copper ferrites depends not only on their initial phase composition, but on the concomitant phase transformations by the influence of the reaction medium.

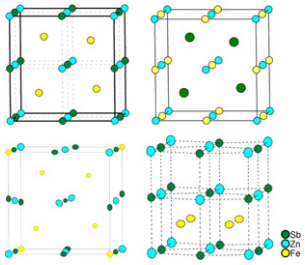

Three types of half-Heusler structure related subunit are identified in the vicinity of the equiatomic composition FeZnSb in the Fe–Zn–Sb system.

Continued

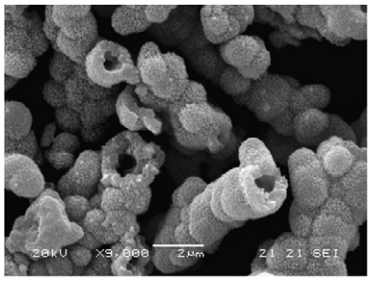

Fe-doped MnO_2 with a hollow sea urchin-like ball chain shape was first synthesized in a high magnetic field of 10 T via a simple chemical process.

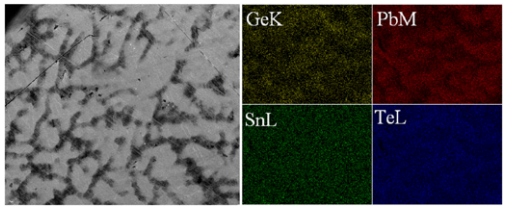

Spinodal decomposition in the GeTe–SnTe–PbTe system demonstrated by SEM and EXS images.

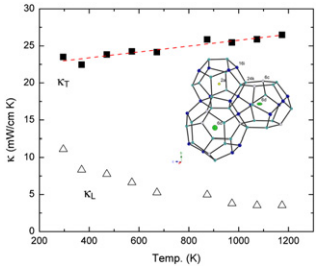

The inorganic type-I clathrate phase with nominal composition $Ba_7Sr_1Al_{14}Si_{32}$ has been prepared by Al flux. Single crystal diffraction at 90 and 12 K reveal that the framework is fully occupied with the cation sites nearly fully occupied. The lattice thermal conductivity is low thereby suggesting further optimization of the carrier concentration will lead to a high zT.

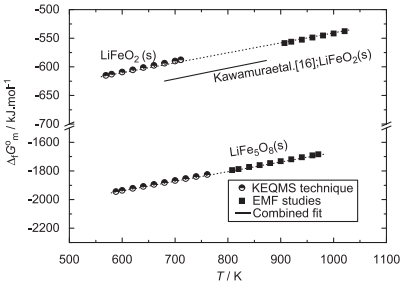

Comparison of $\Delta_f G^o_m(T)$ of lithium ferrites determined using different techniques.

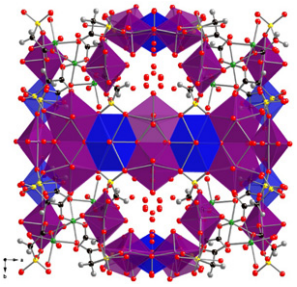

A view of part of the cubic structure of $Cd_2[(UO_2)_6(PO_3CH_2CO_2)_3O_3(OH)(H_2O)_2] \cdot 16H_2O$.

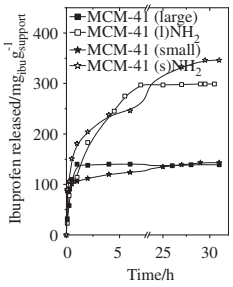

Ibuprofen delivery from the parent and amino-modified spherical MCM-41 materials with 100 nm (small) and 500 nm (large) particle sizes.

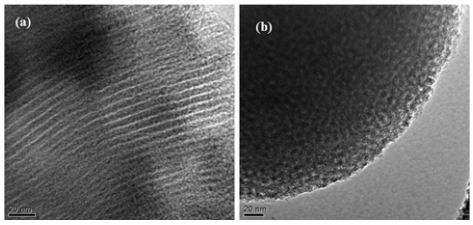

We report the synthesis of new periodic mesoporous organosilicas (PMOs) with the co-existence of diurea and sulfanilamide-bridged organosilica that are potentially useful for controlled drug release system.

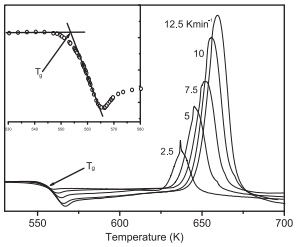

Typical DSC thermogram for TLW glasses for different heating rates with insert graphic showing as the Tg is evaluated.

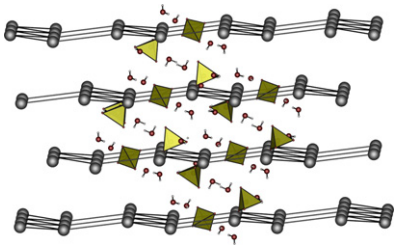

In the lanthanide sulphate octahydrates the cations form slightly undulated layers. Between the layers are voids in which sulphate tetrahedra and water molecules are located. The holmium compound exhibits an Alexandrite effect.

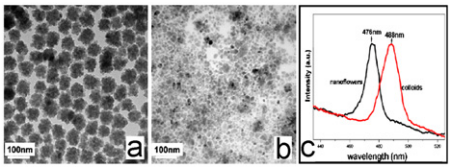

Various $AgGaS_2$ nanocrystals with different morphologies and sizes including 3D nanoflowers (a) and colloids (b) were synthesized in mixed solvent reaction system and their PL spectra was researched (c).

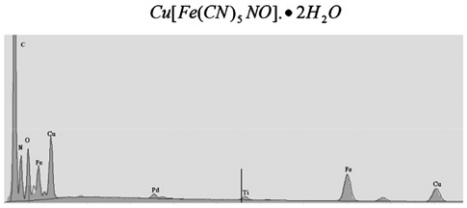

The adsorption space of a very well characterized Cu-nitroprusside polymorph, applying carbon dioxide as probe molecule, was studied.

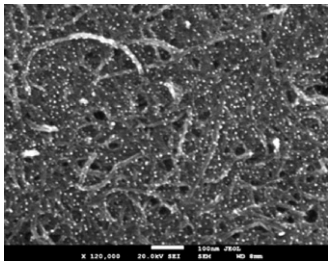

Nickel and nickel oxide nanocrystals were selectively and homogeneously decorated on multiwalled carbon nanotubes using nickel acetylacetonate, as a precursor in a simple and efficient route.

Continued

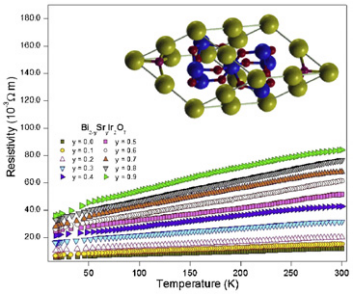

Electrical behavior of the $Bi_{2-y}Sr_yIr_2O_7$ solid solution.

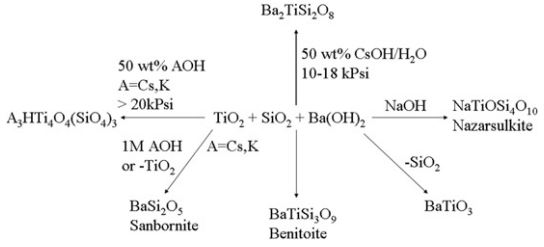

Materials crystallizing from the hydrothermal $TiO_2 + SiO_2 + Ba(OH)_2$ system.

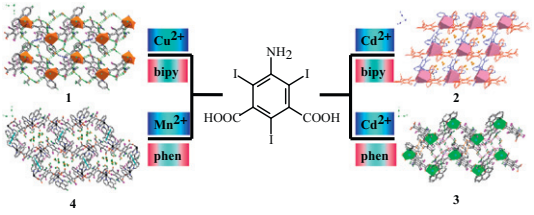

The synthesis, crystal structures and characterization of one 1D homochiral coordination polymer and three achiral 1D coordination polymers with 5-amino-2,4,6-triiodoisophthalic acid (H_2ATIBDC) are reported.

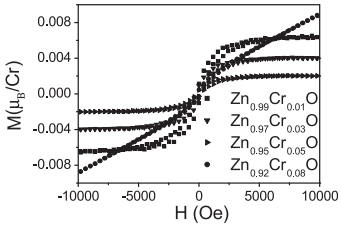

As can be seen from the magnetic hysteresis loops of $Zn_{1-x}Cr_xO$ ($x = 0.01$, 0.03, 0.05, and 0.08) at room temperature under 10 KOe, the samples show good high-T_c ferromagnetism with Cr concentration of less than 5 at%.

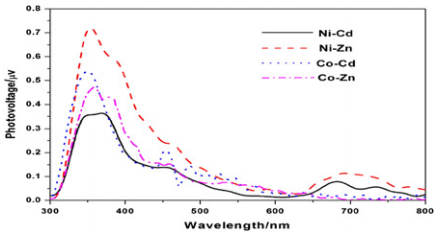

Four heterometallic polymers, Ni–Cd, Ni–Zn, Co–Cd, Co–Zn, were synthesized and characterized. The photoelectric properties of heterometallic polymers were discussed by SPS. The introduction of heterometallic ions will broaden the SPS of corresponded monometallic complexes.

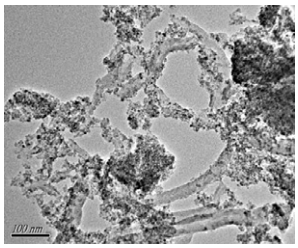

MWCNT/anatase TiO_2 composites have been prepared by a combination of a sol–gel method and a self-assembly technique in one step at low temperature without high temperature calcination.

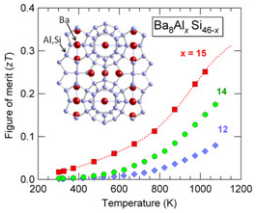

$Ba_8Al_xSi_{46-x}$ is found to crystallize in the type-I clathrate structure without framework deficiency for $8 \le x \le 15$. Thermoelectric figure of merit reaches $zT = 0.24$ for $x = 15$ at 1000 K, and calculation predicts $zT \sim 0.7$ for a lower carrier concentration.

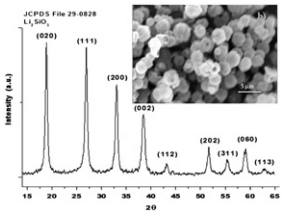

Li_2SiO_3 was synthesized using a hydrothermal process in the presence of different surfactants. Li_2SiO_3 powders were composed of uniform micrometric particles with a hollow sphere morphology and nanostructured walls.

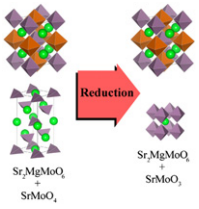

$SrMoO_4$ is formed at low temperatures during the synthesis of Sr_2MgMoO_6, which prevents the volatilization of Mo from typical precursor mixtures of this promising SOFC anode material. $SrMoO_4$ is insulating and it is often found as an impurity in Sr_2MgMoO_6 samples. It is however readily reduced to highly conducting $SrMoO_3$. Composites of Sr_2MgMoO_6 and $SrMoO_3$ show increased electrical conductivities compared to pure Sr_2MgMoO_6 under the reductive operation conditions of an SOFC anode.

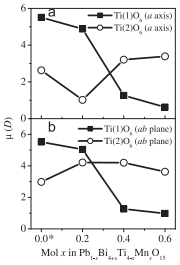

The dipole moment of TiO_6 dependence of x in $Pb_{1-x}Bi_{4+x}Ti_{4-x}Mn_xO_{15}$ ($0 \le x \le 0.6$): (a) along a-axis and (b) on the ab plane. This figure indicated that polarization in the ab-plane contribute to the total polarization.

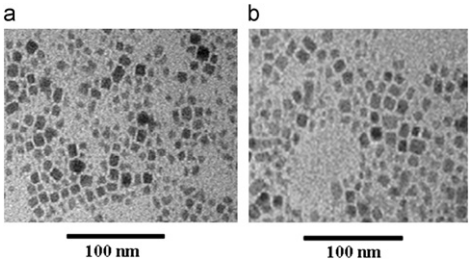

EuS nanoparticles a. before coating and b. after coating.

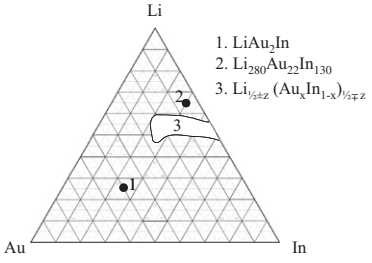

Two real ternary compounds (1: Heusler phase, 2: $n = 6$ variant of a cubic $n \times n \times n$ W-type superstructure) together with one pseudo-ternary compound (3: Zintl phase with its broad homogeneity range).

Continued

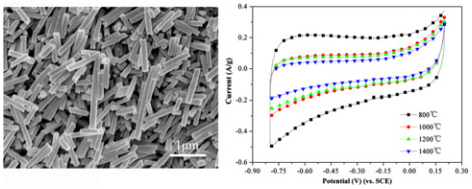

TiN nanorods were prepared using electrospinning followed by thermolysis under different atmospheres. Electrochemical properties of the TiN nanorods showed strong dependence on the nitridation temperature.

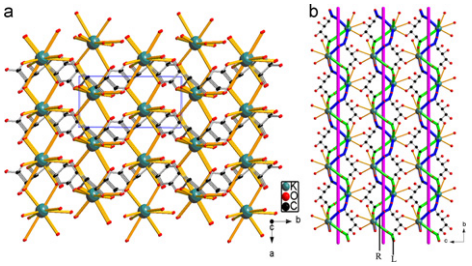

Two K(I) complexes based on D-saccharic acid (H_2sac), $[K(Hsac)]_n$ (**1**) and $[K_2(sac)]_n$ (**2**) were obtained and characterized. Electrochemical studies indicate the potential use of **2** in Ni–MH battery.

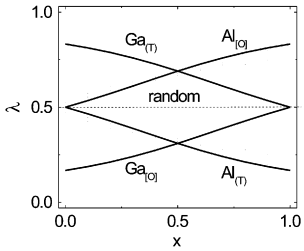

Mullite-type $Bi_2(Ga_xAl_{1-x})_4O_9$ mixed crystals ($0 \le x \le 1$) prepared by a combined mechanochemical–thermal route possess a non-random distribution of Ga^{3+} and Al^{3+} cations over the sites of tetrahedral (*T*) and octahedral [*O*] coordination, characterized by the preference of Ga^{3+} (Al^{3+}) for tetrahedral (octahedral) sites.

Corrigendum